Journal of Computational Physics 310 (2016) 459–477

Contents lists available at ScienceDirect

Journal of Computational Physics

www.elsevier.com/locate/jcp

On the physically based modeling of surface tension and moving contact lines with dynamic contact angles on the continuum scale

M. Huber [a,*], F. Keller [a], W. Säckel [a], M. Hirschler [a], P. Kunz [a], S.M. Hassanizadeh [b], U. Nieken [a]

[a] Institute of Chemical Process Engineering, University of Stuttgart, Boeblinger Str. 78, 70199 Stuttgart, Germany
[b] Department of Earth Sciences, Faculty of Geosciences, Utrecht University, P.O. Box 80021, 3508 TA Utrecht, The Netherlands

ARTICLE INFO

Article history:
Received 17 July 2015
Received in revised form 18 January 2016
Accepted 23 January 2016
Available online 26 January 2016

Keywords:
SPH
Two-phase flow
Surface tension
Moving contact line
Dynamic contact angle
CSF
CLF

ABSTRACT

The description of wetting phenomena is a challenging problem on every considerable length-scale. The behavior of interfaces and contact lines on the continuum scale is caused by intermolecular interactions like the Van der Waals forces. Therefore, to describe surface tension and the resulting dynamics of interfaces and contact lines on the continuum scale, appropriate formulations must be developed. While the Continuum Surface Force (CSF) model is well-engineered for the description of interfaces, there is still a lack of treatment of contact lines, which are defined by the intersection of an ending fluid interface and a solid boundary surface. In our approach we use a balance equation for the contact line and extend the Navier–Stokes equations in analogy to the extension of a two-phase interface in the CSF model. Since this model depicts a physically motivated approach on the continuum scale, no fitting parameters are introduced and the deterministic description leads to a dynamical evolution of the system.

As verification of our theory, we show a Smoothed Particle Hydrodynamics (SPH) model and simulate the evolution of droplet shapes and their corresponding contact angles.

1. Introduction

Although we are familiar with surface tension and subconsciously dealing with it in our daily life, e.g. condensed water droplets on a cold window or water-repellent textiles, the scientific description remains partly ambiguous. Especially with regard to contact angles (CA), which demonstrate the wetting behavior, different models were developed in the past. The static contact angle of a fluid on a plane surface is well described by Young's equation. But if the fluid is in motion, as experiments from Hoffman [1] show, the contact angle changes its value. Blake and Haynes investigated a model based on the molecular-kinetic theory, where adsorption and desorption rates are used to describe the progress of a contact line [2]. A hydrodynamical approach was suggested by de Gennes and Brochard-Wyart [3,4]. They assumed a force balance of the "non-compensated Young Force" and the viscous friction of a Poiseuille flow near a moving contact line. Hereby they also obtained a constitutive relationship between the dynamic contact angle (DCA) and the velocity of the contact line. A further model with an explicit treatment of the surface was proposed by Shikhmurzaev [5]. A comparison of these

* Corresponding author.
E-mail address: manuel.huber@icvt.uni-stuttgart.de (M. Huber).

http://dx.doi.org/10.1016/j.jcp.2016.01.030
0021-9991/

different analytical methods is beyond the scope of this article. Instead we will show a way to include the basic idea of aforementioned approaches and develop a physico-numerical model being able to describe two-phase flow in a capillary or droplet formation with surface tension and contact line movement.

During the last years mesh-free methods fade more and more into spotlight. Despite the higher computational effort compared to grid-based methods and some challenges due to the peculiarity of the method, mesh-free methods are favorable in some applications. One benefit is, they are able to bridge the gap between continuum and fragmentation in a native way. In this manner the description of materials and fluids with complex shapes is predestinated for a particle method with a Lagrangian formulation of the underlying physical process. With respect to multi-phase flow the computational effort does not dramatically increase, because interfaces are not explicitly treated and expensive adaptive spacial resolution for interfaces is not necessary, because the particles move on a continuous scale. A further advantage is the possible treatment of free surfaces which also results in a reduction of the computational effort by only considering the dominating phase.

In the case of laminar multi-phase flow several prerequisites must be achieved to describe the flow pattern of interfaces with contact lines on a microscopical consideration of the continuum scale. Boundary conditions like the no-slip condition give rise to the Hagen–Poiseuille flow profile in a tube for a viscid fluid. The extension by another phase leads to an interfacial balance equation between the two fluid phases. This is where surface tension is introduced. In the Continuum Surface Force model by Brackbill et al. [6] the balance equation is used and reformulated to a volumetric area of influence. Although the treatment of interfaces is nowadays well established, the description of contact lines and corresponding contact angles is still under development.

By now there are in principal four different physico-numerical methods to describe the local wetting behavior on the continuum scale:

1. Static contact angles (DCA with constitutive equation)
2. Slip boundary models
3. Pairwise interaction forces
4. Stress tensor formulations

Method 1 requires a separate description for interfaces and contact lines. The CSF model is commonly used for fluid–fluid interactions and different implementations for contact angles are possible. Liu et al. [7] calculated drop shapes with static contact angles and the wettability of walls using the MPS method. With regard to transport in porous media Ferrari and Lunati [8] simulate two-phase drainage processes using static contact angles and the VOF method. Annapragada et al. [9] calculate droplet shapes on an incline using a static boundary condition for the contact angle with a constitutive equation for the azimuthal angle of the drop. A further constitutive equation is used by Das and Das [10] to obtain volume-dependend contact angles for bigger drops. One has to mention these approaches with static contact angles are sufficient for either stationary problems or dynamical processes with low capillary numbers.

We also put models with constitutive equations for a “dynamic” contact angle in dependence of a contact line velocity in this category, e.g. Sikalo et al. [11], as for a certain configuration of the system the contact angle shall be an input value and not a result of a differential equation. The contact angle itself can be regarded as the boundary condition to the curvature of the interface. Input parameters in these models are static contact angles or advancing/receding contact angles and surface tension coefficients, respectively.

A SPH approach, which imposes static contact angles at the wall, is published by Breinlinger et al. [12]. The idea is to introduce a reset force through an artificially generated curvature in order to obtain static contact angles in equilibrium. The disadvantage of this approach is, a correction of normals at particles close to the wall plus a smoothing is necessary. Moreover, because of a layer dependent formulation, the generated peak curvature may exert a force away from the contact line. Through this procedure a discrepancy between the actual particle arrangement and the imposed particle properties with imposed forces is generated. This is why this force can be seen as an artificial reset force without the claim for correct process dynamics, as the force is not derived from a momentum balance.

Method 2 is a way to incorporate the contact line movement into a slip model for the three-phase contact line, which is necessary to ensure a certain contact angle during the dynamical motion of a system. For a deeper insight we refer to the work of Ren and E [13]. They investigated a slip model with boundary conditions for the moving contact line problem. Input parameters are the static contact angle and an effective friction coefficient for the slip model.

Method 3 is a description for interfaces and contact lines unified in one particle–particle interaction. We want to highlight the work of Tartakovsky and Meakin [14], who first showed an effective formulation of surface tension with accompanying contact angles in SPH. In the same way Zhou et al. [15] used a Lennard-Jones-like potential with adapted coefficients for the use on the continuum scale. An utilization in the Volume of Fluid method is shown by Mahady et al. [16]. This demonstrates the ability in choosing an appropriate, artificial interaction potential and using a fitting parameter as input value to model the qualitative behavior of the physical system. Note that, beside the classical fitting approach, nowadays also theories exist, which derive the coefficients of the pairwise interaction for a use on the continuum scale, see Bandara et al. [17].

Method 4 Lafaurie et al. [18] introduced a multi-phase formulation, which allows for momentum conservation by taking the divergence of the stress-tensor. This leads to a propagation of interfaces and contact lines by a unified description. The

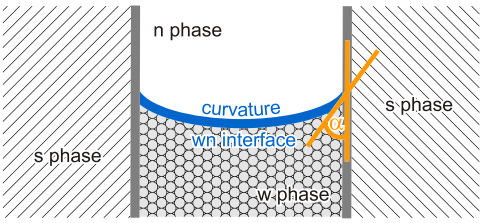

Fig. 1. Schematic illustration of two-phase flow through a capillary, in 2D constrained by solid walls on left and right side. Further important quantities are the curvature κ of the *wn*-interface and the contact angle α as its boundary condition with respect to the solid wall.

first implementation of this method in SPH was published by Hu and Adams [19]. Input parameters are all involved surface tension coefficients.

At low capillary and Bond numbers, surface tension is dominating, and therefore the assumption of a static contact angle is reasonable. At high capillary numbers the viscous flow and body forces are dominating and it might be fair to neglect surface tension completely. But there's a certain range in between where the negligence of the dynamic contact angle would falsify the result. To obtain the dynamic contact angle as a result of a simulation we introduce:

The Contact Line Force model (CLF)

This approach has the potential to easily exchange the driving forces for the contact line and is adjustable to high density ratios.

Balance equations don't merely exist for phases and interfaces, they can also be formulated for contact lines, as Hassanizadeh and Gray [20] showed. From the momentum balance at the contact line we can extend the Navier–Stokes equations in the same way like the CSF model does for an interface. Input parameters are either all three surface tension coefficients or just the static contact angle and the surface tension coefficient of the fluid–fluid interface. The latter are easily characterizable by measurements.

2. Two-phase model

The Navier–Stokes equations for an isothermal, incompressible, single-phase system with a Newtonian fluid in Lagrangian description are given by:

$$\rho \frac{D\mathbf{v}}{Dt} = -\nabla p + \mu \Delta \mathbf{v} + \rho \mathbf{g} \tag{1}$$

$$\frac{1}{\rho}\frac{D\rho}{Dt} = \nabla \cdot \mathbf{v} = 0, \tag{2}$$

where ρ, p and μ are density, pressure and dynamic viscosity. The vectors $\mathbf{v}$ and $\mathbf{g}$ represent velocity and gravitational acceleration. To describe a system as shown in Fig. 1 with regard to two-phase flow and surface tension this model has to be extended.

2.1. The smoothing kernel W

To introduce a smooth transition of the scalar field c from one phase to another, an interpolation technique is applied with kernels usually based on spline functions [21]. Due to stability reasons in our numerical scheme we use the Wendland kernel [22]

$$W(q,h) = \frac{7}{4\pi h^2} \begin{cases} \left(1-\frac{q}{2}\right)^4 (2q+1) & \text{if } q < 2 \\ 0 & \text{else} \end{cases}, \tag{3}$$

with $q = |r|/h$ and the prefactor representing the normalization constant in $2D$, whereas in $3D$ the normalization constant is $21/(16\pi h^3)$. The demand on the kernel is a compact support and in the limit of a vanishing smoothing length h, the kernel has to become the Dirac delta function $\delta(r)$:

$$\int W\left(|\mathbf{r}' - \mathbf{r}|, h\right) d^3 r' = 1\,, \tag{4}$$

$$\lim_{h\to 0} W(r,h) = \delta(r)\,. \tag{5}$$

Because of the incomplete kernel support at domain boundaries, the *mixed kernel and gradient correction* by Bonet and Lok [23] is applied, where the kernel correction is given by

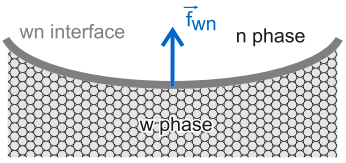

Fig. 2. Continuum surface force at *wn*-interface.

$$W^*\left(|\mathbf{r}' - \mathbf{r}|, h\right) = \frac{W\left(|\mathbf{r}' - \mathbf{r}|, h\right)}{\int W\left(|\mathbf{r}' - \mathbf{r}|, h\right) d^3r'}. \tag{6}$$

With this formulation a scalar field can be interpolated by

$$\widetilde{c}\left(\mathbf{r}, h\right) = \int c\left(\mathbf{r}'\right) W^*\left(|\mathbf{r}' - \mathbf{r}|, h\right) d^3r', \tag{7}$$

and the gradient of $\widetilde{c}(\mathbf{r}, h)$ is obtained by

$$\nabla\widetilde{c}\left(\mathbf{r}, h\right) = \int c\left(\mathbf{r}'\right) \nabla^* W^*\left(|\mathbf{r}' - \mathbf{r}|, h\right) d^3r'. \tag{8}$$

Note that the *mixed kernel and gradient correction* also applies a gradient correction, which is here denoted by ∇^*. With this description it is possible to obtain the fluid-phase interface normal $\mathbf{n}_{wn}$ even close to the solid wall with a proper volume reformulation building the basis of the following description for contact lines.

2.2. Continuum Surface Force model (CSF)

By introducing a second phase, one has to satisfy the interfacial boundary condition [24]

$$(p_w - p_n)\,\hat{\mathbf{n}}_{wn} = (\underline{\underline{\tau}}_w - \underline{\underline{\tau}}_n)\hat{\mathbf{n}}_{wn} - \sigma_{wn}\kappa_{wn}\hat{\mathbf{n}}_{wn} + \nabla\sigma_{wn}, \tag{9}$$

where the indices w, n and later s denote the wetting, the non-wetting and the solid phase. The combination of two of them, e.g. wn, represents an interfacial property like κ_{wn} and σ_{wn}, which denotes the curvature and the surface tension coefficient of the wn-interface. The tensor $\underline{\underline{\tau}}$ represents the viscous stress tensor and $\hat{\mathbf{n}}_{wn}$ is the unit normal to the wn-interface. We assume a constant surface tension coefficient σ_{wn} along the interface, which gives rise to $\nabla\sigma_{wn} = 0$. The normal component of this condition with respect to the interface is responsible for the curvature of this interface. Therefore we include the second term on the right side of Eq. (9) as Continuum Surface Force $\mathbf{f}_{wn}$, see Fig. 2, in our model following the work of Brackbill et al. [6] and calculate the force by

$$\mathbf{f}_{wn} = \sigma_{wn}\kappa_{wn}\hat{\mathbf{n}}_{wn} \tag{10}$$

with a color function c, where each phase has a constant color value and a normal vector of this interface, which is obtained by the gradient of the color function through

$$\mathbf{n}_{wn} = \frac{\nabla\widetilde{c}}{[c]}. \tag{11}$$

$[c]$ denotes the jump in the value of the color function when crossing an interface and can be considered as renormalization. The curvature is further calculated via

$$\kappa_{wn} = -\nabla\cdot\hat{\mathbf{n}}_{wn}. \tag{12}$$

To integrate the CSF model in the Navier–Stokes equations, a volumetric reformulation is applied

$$\mathbf{F}_{wn}^{vol} = \mathbf{f}_{wn}\delta_{wn}, \tag{13}$$

where $|\mathbf{n}_{wn}|$ is used as approximation of the Dirac delta distribution δ_{wn}, due to

$$\int \mathbf{n}_{wn}\cdot d\hat{\mathbf{n}}_{wn} = 1, \tag{14}$$

which is satisfied because of the renormalization $[c]$ in Eq. (11). Thus the Navier–Stokes equations are extended by Eq. (13) and we obtain

$$\frac{D\mathbf{v}}{Dt} = -\frac{1}{\rho}\nabla p + \frac{\mu}{\rho}\Delta\mathbf{v} + \mathbf{g} + \frac{1}{\rho}\mathbf{F}_{wn}^{vol}. \tag{15}$$

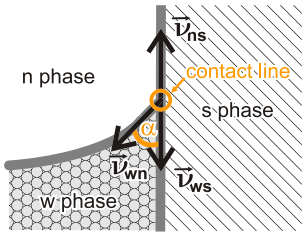

Fig. 3. Contact line with contact angle α.

This formulation is capable of describing a two-phase system, but still cannot handle the contact with a third, solid phase. The advantage of extending the Navier–Stokes equations in this way instead of solving it together with the interface condition is, that we do not explicitly have to describe the interface layer.

Inspired by this approach we come up with a similar description for the three-phase contact area and introduce the Contact Line Force for a dynamical description of evolving contact lines.

2.3. Contact Line Force (CLF)

2.3.1. Momentum balance

Analogous to the derivation of the CSF one can use a balance equation to include the dynamical behavior of the contact line. From the *Microscale Momentum Balance Equation for a Contact Line* by Hassanizadeh and Gray [20] one can derive the *unbalanced Young Force*, as proposed by de Gennes [3]. In this way we introduce a force acting on the contact line, by only balancing interfacial tension, in particular only the component tangential to the solid interface

$$\mathbf{f}_{wns} = \hat{\nu}_{ns}\hat{\nu}_{ns} \cdot \sum_{ij=wn,ns,ws} \sigma_{ij}\hat{\nu}_{ij}\,. \tag{16}$$

Here σ_{ij} denotes the surface tension coefficient of the corresponding interface and $\hat{\nu}_{ij}$ is the tangential unit vector as shown in Fig. 3. We consider the normal component to be in balance, because of the assumption of a fixed solid surface, while the tangential contribution is responsible for the contact line movement along the solid surface. Other formulations of Eq. (16) are given by

$$\mathbf{f}_{wns} = \sigma_{wn}\left[\cos(\alpha_s) - \cos(\alpha_d)\right]\hat{\nu}_{ns}\,, \tag{17}$$

$$\mathbf{f}_{wns} = \left[\sigma_{ns} - \sigma_{ws} + \sigma_{wn}\underbrace{(\hat{\nu}_{ns}\cdot\hat{\nu}_{wn})}_{-\cos(\alpha_d)}\right]\hat{\nu}_{ns}\,, \tag{18}$$

where α_s and α_d denote the static and the dynamic (actual) contact angle. In the equilibrium case $|\mathbf{f}_{wns}| = 0$, Eq. (18) apparently becomes Young's equation

$$\sigma_{ns} = \sigma_{ws} + \sigma_{wn}\cos(\alpha_s). \tag{19}$$

The tangential interface unit vectors $\hat{\nu}_{ij}$ are defined to be orthogonal to the interface normals $\hat{\mathbf{n}}_{ij}$, pointing away from the contact line (in three dimensions orthogonally to the contact line itself), see Fig. 3.

2.3.2. Volume reformulation

Starting at the momentum balance equation for an interface or a contact line the resulting force contribution is in case of the interfacial balance formulated as force per area and in case of the contact line balance as force per line. Hence the role of the volume reformulation is on the one hand a transformation from a force per area/line to a force per volume and on the other hand a redistribution of forces, which act on, e.g. the contact line, to the vicinity of the line. The function δ_{wns}, which will describe this redistribution, therefore is a weighting of Eq. (16) to the region close to the contact line. In case of the CSF, the magnitude of the interface normal is used for the volume reformulation, see Fig. 4(b). There solely is a non-zero contribution in the vicinity of the interface. The volume reformulation for the CLF has to satisfy the same needs, see Fig. 4(d). With the gradient along a direction

$$\nabla_{\nu_{ns}} = \hat{\nu}_{ns}\cdot\nabla \tag{20}$$

we define δ_{wns} in the following way. In a first step the directional derivative is taken tangential to the fluid–solid interface

$$\delta'_{wns}(\mathbf{r}) = \frac{1}{[c]}\nabla_{\nu_{ns}}\widetilde{c} = \hat{\nu}_{ns}\cdot\mathbf{n}_{wn}. \tag{21}$$

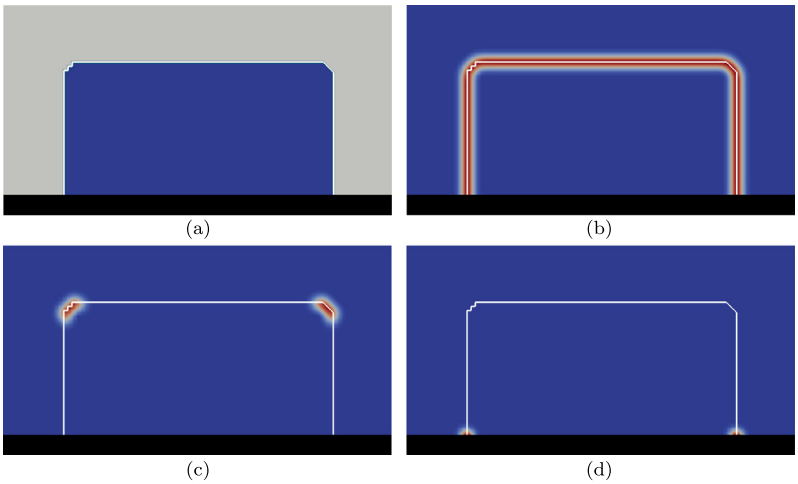

Fig. 4. Initial state, (a) colors represent different phases: solid wall in black, wetting phase in grey and non-wetting phase in blue. (b) Magnitude of fluid phase interface normal $\mathbf{n}_{wn}$, (c) curvature κ and (d) volume reformulation of *CLF*: δ_{wns}. Color scale from blue (zero value) to red with increasing magnitude. (For interpretation of the references to color in this figure legend, the reader is referred to the web version of this article.)

In a second step a further derivative, orthogonal to the previous one, is applied to $\delta'_{wns}(\mathbf{r})$ with direction towards the solid boundary $\hat{\mathbf{d}}_{sx}$

$$\delta_{wns}(\mathbf{r}) = -2\,\nabla_{\mathbf{d}_{sx}}\widetilde{\delta}'_{wns}\,, \tag{22}$$

where the boundary itself is treated as $\delta'_{wns} = 0$ and the derivative is taken with respect to the boundary solely for a well-defined transition right at the boundary, cf. Fig. 4. The factor 2 is introduced, because this volume reformulation is only evaluated and applied to the fluid phase, which represents only half of the kernel support at the contact line. Because $\delta'_{wns} > 0$ inside the fluid domain, the directional derivative towards the outside becomes negative and therefore the minus sign leads to $\delta_{wns} > 0$. Thus we fulfill the condition

$$\iint \delta_{wns}\,d\sigma = 1 \tag{23}$$

$$\text{and } d\sigma = |\mathbf{d}_{sx} \times \nu_{ns}|\; dd_{sx}\,d\nu_{ns}\,, \tag{24}$$

with integration over the fluid domain only. This is stringently required to preserve the quantity of the CLF.

With this knowledge, the volume reformulation of the CLF writes as

$$\mathbf{F}^{vol}_{wns} = \mathbf{f}_{wns}\delta_{wns}. \tag{25}$$

The advantage of this approach is, one is easily able to exchange the driving force $\mathbf{f}_{wns}$ in Eq. (25), if other effective wetting models, e.g. [2], are subject of new investigations.

With Eq. (25) the complete hydrodynamical surface tension model writes as

$$\frac{D\mathbf{v}}{Dt} = -\frac{1}{\rho}\nabla p + \frac{\mu}{\rho}\Delta\mathbf{v} + \mathbf{g} + \frac{1}{\rho}\mathbf{F}^{vol}_{wn} + \frac{1}{\rho}\mathbf{F}^{vol}_{wns}\,, \tag{26}$$

which is capable of describing the dynamics of partial wetting including dynamic contact angles.

3. Time integration

The time integration is solved with a standard second order Leap–Frog scheme, which is given by

$$\mathbf{v}_{n+0.5} = \mathbf{v}_{n-0.5} + \tau\,\mathbf{a}_n \tag{27}$$

$$\mathbf{r}_{n+1} = \mathbf{r}_n + \tau\,\mathbf{v}_{n+0.5}\,, \tag{28}$$

where n denotes the discrete time step, τ the time step interval and $\mathbf{a}$ the complete acceleration according to the momentum balance, cf. Eq. (26). Because this scheme is not self-starting the first step is made by

$$\mathbf{v}_{0.5} = \mathbf{v}_0 + 0.5\,\tau\,\mathbf{a}_0. \tag{29}$$

In this paper the Leap–Frog scheme is used in conjunction with the incompressible SPH scheme. Note that the Leap–Frog scheme for weakly compressible SPH is also used in Liu and Liu [25] and Pan et al. [26].

3.1. Incompressible formulation

To solve the Navier–Stokes equations for incompressible flow, the decomposition of Chorin [27] is used. Hence the following condition in Lagrangian description must be satisfied

$$\frac{d\rho}{dt} = \rho \nabla \cdot \mathbf{v} = 0\,. \tag{30}$$

As a consequence a divergence-free velocity field is demanded for time integration. By taking the divergence of Eq. (27), we obtain

$$0 = \nabla \cdot \left(\mathbf{v}_{n-0.5} + \tau \left(\frac{\mu}{\rho} \Delta \mathbf{v} + \mathbf{g} + \frac{1}{\rho} \mathbf{F}_{wn}^{vol} + \frac{1}{\rho} \mathbf{F}_{wns}^{vol} \right)_n \right) - \tau \, \nabla \cdot \left(\frac{1}{\rho} \nabla p \right)_n , \tag{31}$$

which is the pressure-Poisson equation

$$\frac{1}{\tau} \nabla \cdot \mathbf{v}_{int} = \nabla \cdot \left(\frac{1}{\rho} \nabla p \right)_n . \tag{32}$$

By this means we have to solve a linear equation system, which couples the whole computational domain to obtain the pressure field. Note that in the first step $\tau \rightarrow \tau/2$, because of Eq. (29). The libraries we use are the algebraic multigrid preconditioner BoomerAMG from hypre [28,29] and the BiCGStab method from PETSc [30–32].

3.2. Resulting predictor–corrector scheme

This leads to a predictor–corrector scheme. The intermediate velocity in the predictor step is given by

$$\mathbf{v}_{int} = \mathbf{v}_{n-0.5} + \tau \left(\frac{\mu}{\rho} \Delta \mathbf{v} + \mathbf{g} + \frac{1}{\rho} \mathbf{F}_{wn}^{vol} + \frac{1}{\rho} \mathbf{F}_{wns}^{vol} \right)_n \tag{33}$$

and

$$\mathbf{v}_n = \mathbf{v}_{n-0.5} + \frac{\tau}{2} \mathbf{a}_{n-1}\,. \tag{34}$$

Therewith the pressure-Poisson Eq. (32) is solved and the hereby obtained pressure field is used to accomplish the corrector step

$$\mathbf{v}_{n+0.5} = \mathbf{v}_{int} - \tau \left(\frac{1}{\rho} \nabla p \right)_n . \tag{35}$$

After that the positions are updated through Eq. (28).

3.3. Time step criteria

For stability reasons several time step criteria must be fulfilled, the Courant–Friedrichs–Lewy (CFL) criterion

$$\tau \leq 0.1 \frac{l_0}{|\mathbf{v}|_{max}}\,, \tag{36}$$

with l_0 as initial particle spacing and $|\mathbf{v}|_{max}$ as the maximum velocity in the computational domain and additionally a viscous diffusion condition

$$\tau \leq 0.1 \frac{l_0^2}{\eta_{max}}\,, \tag{37}$$

with $\eta = \mu/\rho$ as kinematic viscosity, and with η_{max} denoting the maximum kinematic viscosity of all involved particles. To take care of external forces and surface tension forces, respectively, the CFL criterion is not only applied for the complete time step, but also for the predictor with $|\mathbf{v}|_{max} = max\,(|\mathbf{v}_{int}|)$.

4. Implementation in SPH

We dispense with a general introduction into Smoothed Particle Hydrodynamics and instead refer to some fundamental work to look up. The first publications by Lucy [33] and Gingold and Monaghan [34] aimed for the description of astrophysical phenomena. With respect to a more general formulation and application of SPH however, a suitable overview is given by Monaghan [35] and Rosswog [36]. Due to the similarity of astrophysics and fluid-dynamics, soon other applications were found. With regard to single-phase flow a crucial issue is the no-slip boundary condition, which was first verified by Morris et al. [37] for a fluid–solid interface with discretized solid particles. The extension by a second phase demands some classical two-phase flow validations like Rayleigh–Taylor instabilities, see Szewc et al. [38], or rising bubbles, as shown by Colagrossi and Landrini [39]. Other test cases involve Kelvin–Helmholtz instabilities, see Price [40] and Read et al. [41], or Taylor–Green vortices and lid-driven cavities, see Hu and Adams [42] and Adami et al. [43]. From an application perspective, modeling high density ratios is of special interest. With this in view, Grenier et al. [44,45] published a SPH-formulation to describe real water/gas-interfaces. A promising approach with respect to surface tension is published by Hu and Adams [19], which allows for a momentum conserving formulation. For a separate description of interface dynamics and contact line dynamics, we use the well-established SPH-formulation of the CSF model by Morris [46]. An adjusted description for the interface is shown by Adami et al. [47] to take high density ratios in the CSF model into account.

With respect to contact line dynamics we introduce a formulation for the Contact Line Force, which completes the interaction of the CSF model when the two-phase interface approaches the third, solid phase.

4.1. Mixed kernel and gradient correction [23]

To guarantee zero order consistency the Shepard correction is applied to the kernel of Eq. (3) and therefore the corrective SPH kernel writes as

$$W^*(r_{ab},h) = \frac{W(r_{ab},h)}{\sum_b V_b\, W(r_{ab},h)}, \tag{38}$$

with $r_{ab} = |\mathbf{r}_a - \mathbf{r}_b|$ and $V_b = m_b/\rho_b$. Using the quotient rule the gradient of the corrected kernel becomes

$$\nabla W^*(r_{ab},h) = \frac{\nabla W_{ab} - W_{ab}\sum_b V_b\,\nabla W_{ab}/\xi_a}{\xi_a}, \tag{39}$$

with the normalization $\xi_a = \sum_b V_b\, W_{ab}$ and $W_{ab} = W(r_{ab},h)$. Further the gradient correction is applied to satisfy rotational invariance, which results in the final corrected gradient of the kernel

$$\nabla^* W^*(r_{ab},h) = \underline{\underline{L}}_a \nabla W^*(r_{ab},h) \tag{40}$$

with the matrix

$$\underline{\underline{L}}_a = \left(\sum_b V_b \nabla W^*_{ab} \otimes \mathbf{r}_{ba}\right)^{-1}. \tag{41}$$

4.2. Navier–Stokes equations

The viscous model is taken from Szewc et al. [48]

$$(\nabla(\eta\nabla\cdot\mathbf{v}))_a = \sum_b \xi_{ab}\mathbf{v}_{ab}\cdot\mathbf{r}_{ab}\nabla^*_a W^*_{ab} \tag{42}$$

$$= \sum_b 8 m_b \frac{\eta_a+\eta_b}{\rho_a+\rho_b}\frac{\mathbf{v}_{ab}\cdot\mathbf{r}_{ab}}{|\mathbf{r}_{ab}|^2+\zeta^2}\nabla^*_a W^*_{ab}, \tag{43}$$

with $\mathbf{v}_{ab} = \mathbf{v}_a - \mathbf{v}_b$ representing the velocity difference of particle a and b. $\zeta = 0.01h$ is a small numerical parameter, preventing the denominator to become zero.

Further the pressure term in the momentum balance is discretized by

$$\left(\frac{1}{\rho}\nabla p\right)_a = \sum_b m_b \frac{p_a+p_b}{\rho_a\rho_b}\nabla^*_a W^*_{ab}, \tag{44}$$

which was already used in this way by Morris [46] and Colagrossi and Landrini [39].

To be mass conserving, the multi-phase formulation for the density by Hu and Adams [19] is used

$$\rho_a = m_a \sum_b W_{ab}. \tag{45}$$

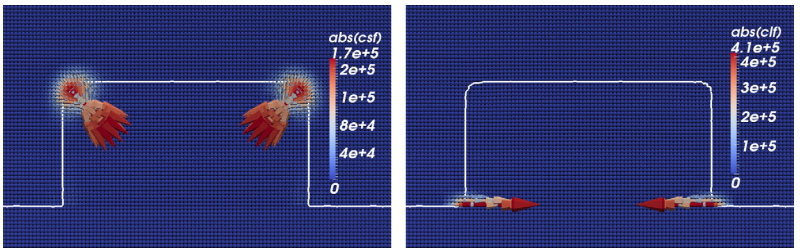

(a) (b)

Fig. 5. Initial state: (a) Visualization of the Continuum Surface Force (CSF). (b) Visualization of the Contact Line Force (CLF). Static contact angle is set to 140°.

The projection method of Cummins and Rudman [49] leads to a SPH-formulation of the pressure-Poisson equation with the left-hand side

$$\left(\nabla\cdot\left(\frac{1}{\rho}\nabla p\right)\right)_a = \sum_b \chi_{ab} p_{ab} = \sum_b V_b \frac{4}{\rho_a+\rho_b}\frac{\mathbf{r}_{ab}\cdot\nabla_a^* W_{ab}^*}{|\mathbf{r}_{ab}|^2+\zeta^2} p_{ab} \tag{46}$$

of the linear equation system. p_{ab} denotes the pressure difference of particle a and b with $p_{ab} = p_a - p_b$. The right-hand side is described by

$$\frac{1}{\tau}(\nabla\cdot\mathbf{v}_{int})_a = \frac{1}{\tau}\sum_b V_b\left(\mathbf{v}_{int_b} - \mathbf{v}_{int_a}\right)\cdot\nabla_a^* W_{ab}^*\,. \tag{47}$$

4.3. Surface tension

As we are now only considering the *wn*-interface we reduce for readability reasons the denotation of interface normal and curvature for particle a from $\mathbf{n}_{wn_a}$ to $\mathbf{n}_a$, and in the same way $\nu_a = \nu_{ns_a}$. The interface normal is evaluated through the jump in the color function according to

$$\mathbf{n}_a = \frac{1}{[c]}\sum_b V_b\,(c_b - c_a)\,\nabla_a^* W_{ab}^*. \tag{48}$$

The unit normal is further used to calculate the curvature κ through

$$\kappa_a = -\sum_b V_b\left(\hat{\mathbf{n}}_b - \hat{\mathbf{n}}_a\right)\cdot\nabla_a^* W_{ab}^*\,, \tag{49}$$

where the summation only includes particles with $|\mathbf{n}| > 0.01/h$. Therewith the surface force writes as

$$\mathbf{F}_{wn_a}^{vol} = \sigma_{wn}\kappa_a\mathbf{n}_a\,. \tag{50}$$

The result is shown in Fig. 5(a), the stronger the curvature, the stronger the continuum surface force. To determine the dynamic contact angle α_d, the distance vector

$$\mathbf{d}_a = \sum_b V_b\,\mathbf{r}_{ba}\,W_{ab}^* \tag{51}$$

is used, which points straight to the wall, where summation is only applied over solid boundary particles or ghost particles. This approximation is satisfying as only the direction and not the magnitude is relevant for further processing. $\hat{\mathbf{d}}_a\cdot\hat{\mathbf{n}}_a = cos(\alpha)$ describes the contact angle of that phase, the interface normal $\hat{\mathbf{n}}_a$ is pointing at, and therefore it is the contact angle of the phase with the higher color value c. Thus $\hat{\mathbf{d}}_a\cdot\hat{\mathbf{n}}_a = -cos(\alpha_d)$ represents the contact angle of the other phase with lower color value. Eq. (17) or (18) is applied by

$$\mathbf{f}_{wns_a} = \sigma_{wn}\left[cos(\alpha_s) + \hat{\mathbf{d}}_a\cdot\hat{\mathbf{n}}_a\right]\hat{\nu}_a, \tag{52}$$

with

$$\nu_a = |\mathbf{d}_a|^2\,\mathbf{n}_a - (\mathbf{d}_a\cdot\mathbf{n}_a)\,\mathbf{d}_a\,. \tag{53}$$

This means only two parameters, the surface tension coefficient σ_{wn} and the static contact angle α_s of one phase, namely the one with the lower color value due to the choice of the "+"-sign in Eq. (52), are necessary as input parameters for the dynamic two-phase model with a solid boundary. Note that with this formulation ν_a does not necessarily point in

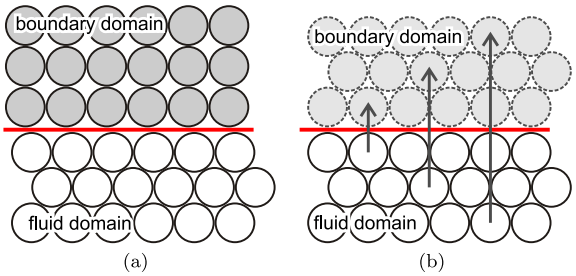

Fig. 6. Different boundary methods: (a) Fluid particles move while boundary is discretized by fixed solid particles. (b) Boundary particles dynamically generated by mirroring of fluid particles, known as ghost particle method.

the direction away from the wetting phase, tangential to the interface of solid and non-wetting phase, as shown in Fig. 3. Through this definition it points away from the phase with lower color value, tangential to the interface of solid phase and the phase with higher color value.

The volume reformulation of the *CLF* is given by Eq. (22). With the directional derivative we obtain

$$\delta_{wns_a} = -2\,\hat{\mathbf{d}}_a \cdot \sum_b V_b \left(\delta'_{wns_b} - \delta'_{wns_a}\right) \nabla^*_a W^*_{ab} \tag{54}$$

with

$$\delta'_{wns_b} = \begin{cases} \delta'_{wns_a} & \text{if } b \in \mathit{fluid} \\ 0 & \text{if } b \in \mathit{boundary} \end{cases} \tag{55}$$

and

$$\delta'_{wns_a} = \hat{\nu}_a \cdot \mathbf{n}_a\,, \tag{56}$$

where the boundary can be described by solid particles and ghost particles, respectively. Due to the definition $\delta'_{wns_a} > 0$. Therewith the volume reformulation for the *CLF* is given by

$$\mathbf{F}^{vol}_{wns_a} = \mathbf{f}_{wns_a} \delta_{wns_a}\,, \tag{57}$$

and its illustration is shown in Fig. 5(b). The stronger the deviation to the static contact angle, the stronger the contact line force.

4.4. Boundary conditions

The boundary treatment is a crucial aspect of any SPH model. Depending on the geometry and complexity of the boundary structure, there are different ways how boundary conditions can be implemented. Due to this choice and the corresponding approximation error, these formulations exert a significant influence on the solution, not only close to the boundary, but also within the computational domain and furthermore influence the stability of the method, see Basa et al. [50]. Several higher order methods were proposed to improve convergence and accuracy, cf. Belytschko et al. [51]. Derivative approximations can be corrected for example by considering Taylor series expansion with higher-order terms, see Chen et al. [52] and Zhang and Batra [53], respectively. Another approach for instance is to use a moving least-squares approximation as published by Liu et al. [54] and Bilotta et al. [55]. One can usually say the higher the considered order for approximation, the better the result, but in turn the higher the computational effort as well. This is why we chose the method of Bonet and Lok [23], which represents a satisfying compromise for the applications below.

This method compensates the particle deficiency close to a boundary and therefore is an appropriate way to calculate the normal of an interface close to the contact line.

4.4.1. Velocity boundary condition

To impose reference values through a Dirichlet boundary condition on a flat interface of fluid and boundary domain, Cummins and Rudman [49] proposed the ghost particles method, see Fig. 6(b). There ghost particles obtain the velocity

$$\mathbf{v}^g_b = 2\mathbf{v}_{ref} - \mathbf{v}_b \tag{58}$$

for example to enforce the reference value $\mathbf{v}_{ref}$ right on the interface. A more detailed explanation can be found in Szewc et al. [48]. Neumann boundary conditions like $\frac{dv_x}{dn} = 0$ are applied by setting

$$v^g_{b_x} = v_{b_x}\,, \tag{59}$$

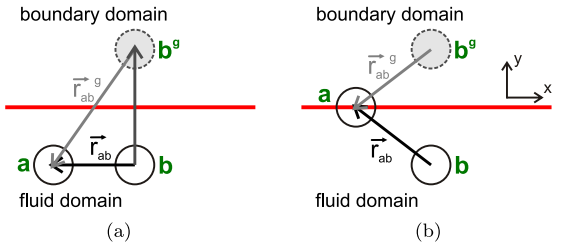

Fig. 7. Mirroring of ghost particles: (a) Generation of ghost distance vector $\mathbf{r}_{ab}^{g}$ and (b) illustration in the limit of particle a coming close to the boundary itself.

which can be used for every desired component. Also a component-by-component composition of Dirichlet and Neumann boundary condition is possible for a vector field.

Note that using an approach for the momentum balance, for instance as suggested by Adami et al. [47,56]

$$(\nabla(\eta\nabla\cdot\mathbf{v}))_a = \frac{1}{m_a}\sum_b \left(V_a^2+V_b^2\right)\frac{2\mu_a\mu_b}{\mu_a+\mu_b}\frac{\mathbf{v}_{ab}}{|\mathbf{r}_{ab}|^2+\zeta^2}\mathbf{r}_{ab}\cdot\nabla_a W_{ab}\,, \tag{60}$$

this traditional description of boundary conditions, cf. Eqs. (58)/(59), is sufficient.

Special treatment of the velocity boundary condition If the viscous contribution is formulated by Eq. (43) the traditional description is also sufficient for homogeneous flows close to the boundary like the Poiseuille flow but can lead to instabilities when velocity components normal to the wall and irregular particle arrangements are present in the immediate vicinity of the wall. An explanation can be found in the following. To recapitulate Eq. (43) and reducing it to the substantial contribution without kernel and gradient correction we formulate this equation for the boundary interaction in the following way

$$\begin{aligned}(\nabla(\eta\nabla\cdot\mathbf{v}))_a &= \sum_{b\cup b^g}\xi_{ab}\mathbf{v}_{ab}\cdot\mathbf{r}_{ab}\nabla_a W_{ab}\\ &= \sum_b \xi_{ab}\left(v_{ab_x}r_{ab_x}+v_{ab_y}r_{ab_y}\right)\nabla_a W_{ab}+\sum_{b^g}\xi_{ab}^{g}\left(v_{ab_x}^{g}r_{ab_x}^{g}+v_{ab_y}^{g}r_{ab_y}^{g}\right)\nabla_a W_{ab}^{g}\,.\end{aligned} \tag{61}$$

Notice that particle a is also mirrored at the domain boundary and its ghost particle belongs to the group of neighboring ghost particles b^g.

The ghost distance vector $\mathbf{r}_{ab}^{g}$ of particle a and ghost particle b^g is in general calculated according to Fig. 7(a). Considering this boundary condition in the limit of particle a sitting right at the boundary (see Fig. 7(b)), one obtains

$$(\nabla(\eta\nabla\cdot\mathbf{v}))|_{wall_a} = \sum_b \frac{\xi_{ab}}{r_{ab}}\left(v_{ab_x}r_{ab_x}+v_{ab_y}r_{ab_y}\right)\begin{bmatrix} r_{ab_x}\frac{\partial W}{\partial r}\\ r_{ab_y}\frac{\partial W}{\partial r}\end{bmatrix} \tag{62}$$

$$+\sum_b \frac{\xi_{ab}}{r_{ab}}\left(v_{ab_x}^{g}r_{ab_x}-v_{ab_y}^{g}r_{ab_y}\right)\begin{bmatrix} r_{ab_x}\frac{\partial W}{\partial r}\\ -r_{ab_y}\frac{\partial W}{\partial r}\end{bmatrix}, \tag{63}$$

with $r_{ab_x}^{g}=r_{ab_x}$ and $r_{ab_y}^{g}=-r_{ab_y}$.

The traditional way to reach a no-slip boundary condition by setting $\mathbf{v}_b^g=-\mathbf{v}_b$, results in

$$(\nabla(\eta\nabla\cdot\mathbf{v}))|_{wall_a} = \sum_b 2\frac{\xi_{ab}}{r_{ab}}\begin{bmatrix}\left(v_{a_x}r_{ab_x}-v_{b_y}r_{ab_y}\right)r_{ab_x}\frac{\partial W}{\partial r}\\ \left(v_{a_y}r_{ab_y}-v_{b_x}r_{ab_x}\right)r_{ab_y}\frac{\partial W}{\partial r}\end{bmatrix}. \tag{64}$$

For instance setting the internal velocity field to a value of $\mathbf{v}=[v(\mathbf{r}),\,0]$, the y-component of Eq. (64) results in general in a non-zero value, which means although there is no velocity in y-direction the viscosity causes an acceleration in y-direction. This unphysical behavior is caused all over the domain. To get rid of this at the boundary, where a real no-slip condition prevents the particle from penetrating the boundary, we set $\mathbf{v}_b^g=[-v_{b_x},\,v_{b_y}]$ as boundary condition for the x-component and $\mathbf{v}_b^g=[v_{b_x},\,-v_{b_y}]$ as boundary condition for the y-component. By this we obtain

$$(\nabla(\eta\nabla\cdot\mathbf{v}))|_{wall_a} = \sum_b 2\frac{\xi_{ab}}{r_{ab}}\begin{bmatrix} v_{a_x}r_{ab_x}r_{ab_x}\frac{\partial W}{\partial r}\\ v_{a_y}r_{ab_y}r_{ab_y}\frac{\partial W}{\partial r}\end{bmatrix}, \tag{65}$$

which has no y-component for $\mathbf{v}=[v(\mathbf{r}),\,0]$.

Note that this result in square brackets is now comparable to the result of Eq. (60) right at the boundary.

The mirror approach in general is valid for other quantities of the momentum balance like pressure, e.g., or the density as well.

4.4.2. Pressure boundary condition

With respect to pressure in ISPH the boundary condition is splitted and has to be considered on the one hand in the pressure Poisson Eq. (32) and on the other hand in the corrector step by Eq. (35). To incorporate the Dirichlet boundary condition in the pressure Poisson equation, the interaction of ghost particles is added to the regular interaction. Due to $p^g_{ab} = p_a - p^g_b = p_a - 2p_{ref} + p_b$ the adjusted formulation for the pressure Poisson equation is

$$\sum_b \chi_{ab}(p_a - p_b) + \sum_{b^g} \chi^g_{ab}(p_a + p_b) = \frac{1}{\tau}\sum_b V_b \mathbf{v}_{int_{ba}} \cdot \nabla^*_a W^*_{ab} + \frac{1}{\tau}\sum_{b^g} V_b \mathbf{v}^g_{int_{ba}} \cdot \nabla^*_a W^{g*}_{ab} + \sum_{b^g} 2\chi^g_{ab} p_{ref} \,. \tag{66}$$

The Neumann boundary condition $\frac{dp}{dn} = 0$ is realized because of $p^g_{ab} = p_a - p^g_b = p_a - p_b$ through

$$\sum_b \chi_{ab}\,(p_a - p_b) + \sum_{b^g} \chi^g_{ab}\,(p_a - p_b) = \frac{1}{\tau}\sum_b V_b \mathbf{v}_{int_{ba}} \cdot \nabla^*_a W^*_{ab} + \frac{1}{\tau}\sum_{b^g} V_b \mathbf{v}^g_{int_{ba}} \cdot \nabla^*_a W^{g*}_{ab} \,. \tag{67}$$

In both ways the right hand side of the pressure Poisson equation requires a boundary condition for the divergence of the velocity field, which is realized through $\mathbf{v}^g_{int_b} = [v_{int_b,x}, -v_{int_b,y}]$.

Periodic boundary conditions with an additional Δp can be applied in the same way by using

$$p^p_{ab} = p_a - p^p_b = p_a - (p_b + \Delta p) = p_a - p_b - \Delta p \,. \tag{68}$$

After solving the linear equation system these pressure values $p^{p/g}_b$ are also used in Eq. (44) of the corrector step.

4.4.3. Boundary condition for surface tension

To prevent the particles from penetrating the wall due to surface tension one has to guarantee, that no force contribution normal to a wall is left

$$\mathbf{d}_a \cdot \mathbf{F}^{vol}_{wn_a} \stackrel{!}{=} 0 \,. \tag{69}$$

In case of fixed boundary particles, cf. Fig. 6(a), the fluid–solid interaction is described as introduced by Morris [37]. The wall is discretized by solid particles and with respect to a no-slip boundary condition, the boundary particles obtain a fictitious velocity to ensure $v = 0$ on the wall. These boundary particles are also used to ensure no fluid particles will penetrate the wall by solving the pressure on the boundary particles, too. Thus the pressure gradient keeps the fluid particles in the fluid domain due to the incompressibility criterion.

Alternative approaches for explicit boundary treatment can be found in Ferrand et al. [57], Mayrhofer et al. [58] and Vacondio et al. [59], respectively.

5. Results

5.1. Time integration scheme

The new integration scheme is compared to the well-established Euler-method, which is for instance used in Shao and Lo [60]. The initial state is a rectangle, filled by 100×50 particles, all of the same phase. On top and bottom a free slip condition is applied. At the bottom a Neumann boundary condition for pressure $\frac{\partial p}{\partial n} = 0$ is applied and on top a Dirichlet condition $p_{top} = p(x)$ is used, which has the same pressure gradient along the width as is imposed on left and right side, see Fig. 8(a). The pressure difference from left to right is calculated in analogy to a spring pendulum by

$$\Delta p(t) = p_0 \cdot (x(t) - x_0) \text{ with } p_0 = 4\pi^2 \frac{\rho L_x}{T^2} \,, \tag{70}$$

where L_x and T are length in x-direction and cycle duration, respectively. Particles can move periodically from left to right and vice versa. The result for $T = 1$ s, $L_x = 0.01$ m and $\rho = 1000$ kg/m^3 is shown in Fig. 8(b)–(f). The total energy is calculated according to the pendulum by

$$E_{tot} = 2\pi^2 \frac{V\rho}{T^2}(x - x_0)^2 + \frac{1}{2} m v^2 \,. \tag{71}$$

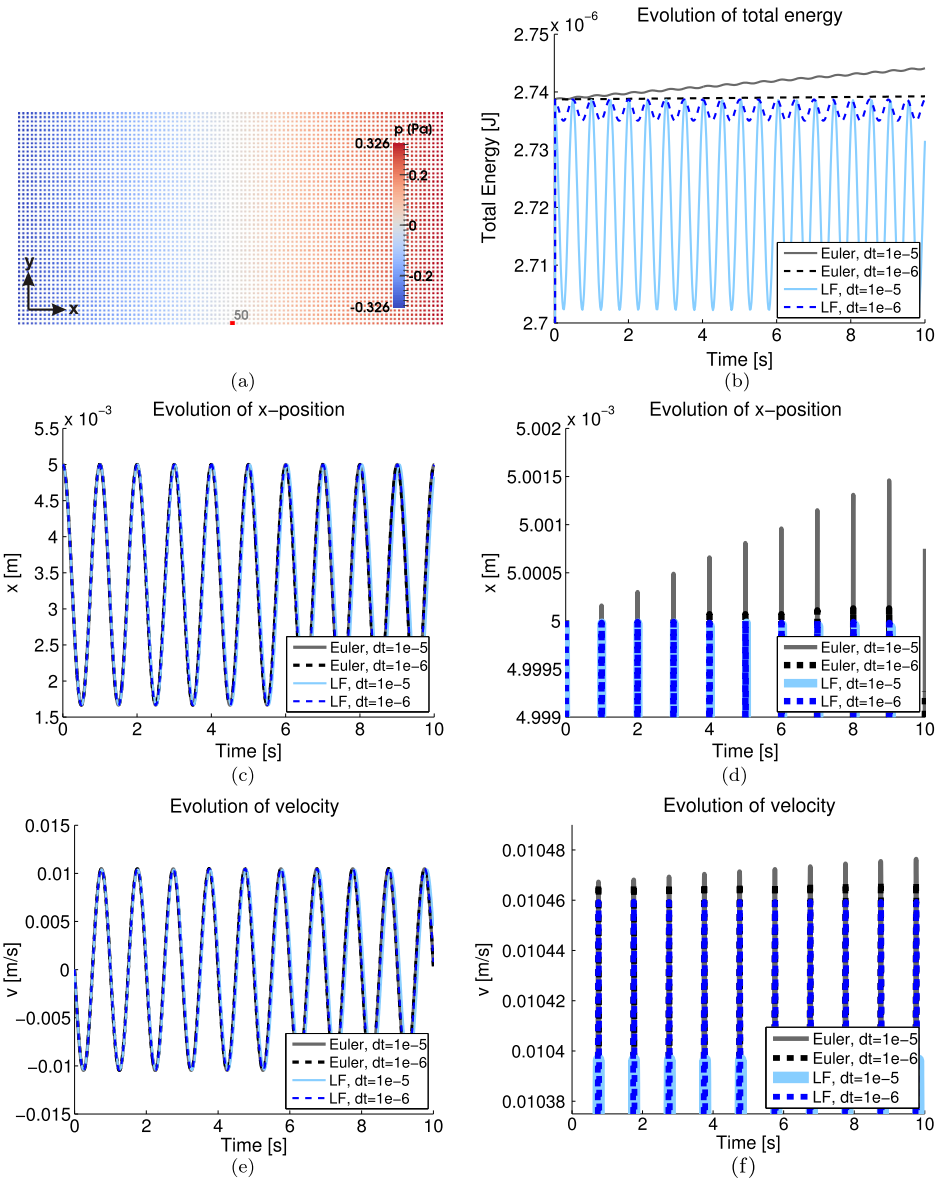

Fig. 8. (a) shows the relative pressure field, which varies in time due to the particle elongation with respect to the reference position. (b) shows the resulting time series of the total energy of the system for the two different integration schemes with two different time step sizes each.

The Leap–Frog scheme shows an oscillating behavior of the total energy, which is caused by the periodic transfer of kinetic energy to potential energy and back. This behavior is well-known for Verlet-methods in periodic regimes and reflects our expectations. In contrast to the integration scheme used in Shao and Lo [60] the total energy of the Leap–Frog scheme is bounded. A reduction of the time increment reduces the oscillating behavior of the total energy, whereas in the Euler-method the divergent behavior is damped.

5.2. Surface tension

To look at wetting processes with the new CLF we analyze droplet shapes, where we first look at a droplet relaxation on a solid wall, cf. Fig. 9. The initial phase distribution is shown in (a). Surface tension is pushing the system towards an energetic minimum state, which means the equilibrium contact angle has to be achieved in combination with a homogeneously curved interface with minimal interfacial area between both phases. In this model the CLF is responsible for the motion of the contact line, which adjusts a new contact angle. The magnitude of the CLF is depending on the difference of actual and static CA, cf. Eq. (17). Therefore an initial contact angle, which is not equal to the static contact angle, will give rise to a CLF, which will cause the motion of the contact line until the static contact angle is achieved. Hence, the consequence of

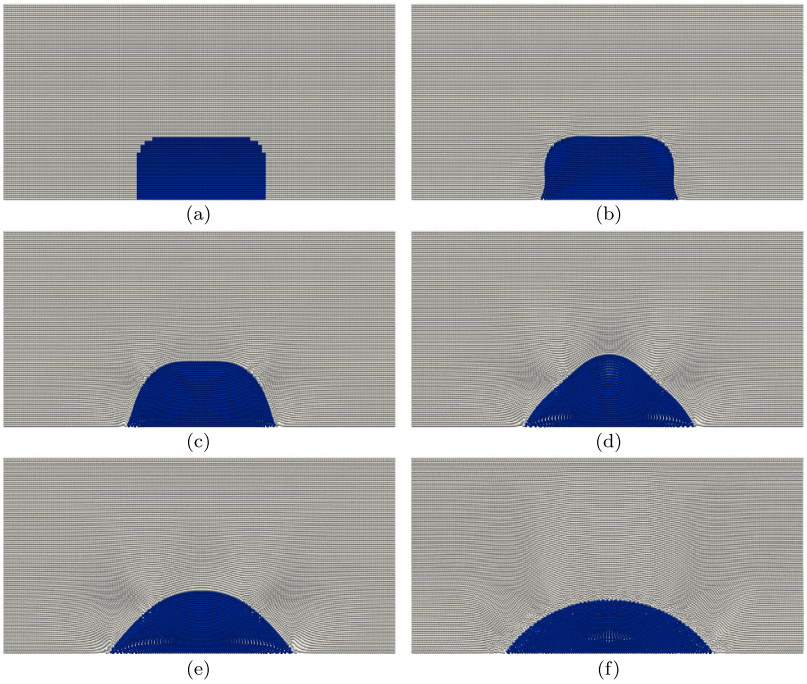

Fig. 9. Evolution of drop formation. Both phases have the same densities $\rho_1 = \rho_2 = 1000$ kg/m^3, the dynamic viscosities are set to $\mu_1 = \mu_2 = 0.01$ kg/s m and the surface tension is set to $\sigma_{wn} = 0.0182$ N/m with a static contact angle of $\alpha_s = 50°$. (a) Shows the initial state, and further states are shown after (b) 2 µs, (c) 5 µs, (d) 10 µs, (e) 20 µs and finally (f) at rest after 200 µs. The computational domain is set to $\Delta x = 0.01$ m, $\Delta y = 0.005$ m and is discretized by 200×100 particles.

an initial droplet shape as shown in Fig. 9(a) and a static contact angle of $\alpha_s = 50°$ is a transient motion with dynamic contact angles. The temporal evolution of this process is shown in (b)–(e) and the equilibrium state with the droplet at rest is shown in (f). The results of different simulations with other static contact angles are shown in Fig. 10. The absolute errors of these equilibrium states compared to their set values are shown in Fig. 11(a). The error in the partial wetting regime between 30°–140° is below 5%. The contact angle is hereby calculated through

$$\alpha_{cl} = \frac{1}{\sum_b \delta_{wns_b}} \sum_b \alpha_b \, \delta_{wns_b} \, . \tag{72}$$

After the drop has reached its equilibrium state, a pressure gradient of $\frac{dp}{dx} = -200 \ \frac{\text{Pa}}{\text{m}}$ is applied, to show steady state advancing and receding contact angles under a constant motion of the drop, see Fig. 11(b). The temporal evolution of the advancing and receding contact angle together with the apex height is shown in Fig. 12(a). This approach leads to a linear dependency of the dynamic contact angle on the contact line velocity in the limited range around the static contact angle, see Fig. 12(b). This result was achieved using several simulations with pressure gradients ranging from $\frac{dp}{dx} = -500 \ \frac{\text{Pa}}{\text{m}}$ to $\frac{dp}{dx} = 0 \ \frac{\text{Pa}}{\text{m}}$, each simulation resulting in a steady state droplet shape under constant motion to the right and one advancing and one receding contact angle. The contact line velocity is hereby determined with

$$\mathbf{r}_{cl} = \frac{1}{\sum_b \delta_{wns_b}} \sum_b \mathbf{r}_b \, \delta_{wns_b} \quad \text{and} \quad \mathbf{v}_{cl} = \frac{d\mathbf{r}_{cl}}{dt} \, . \tag{73}$$

Note that also static contact angles below 30° and above 140° are applicable. The CLF will calculate the correct driving force, but despite the higher order method of Eq. (40), the interface will be badly resolved by a few particles due to the narrow tips in these strong wetting or non-wetting regimes and therefore the normal at the contact line will lose accuracy. This is why the error plot of Fig. 11(a) increases when it comes to strong wetting or non-wetting regimes. If one has a look at the "grid convergence", we realize that the error of the static contact angle does not decrease but converge while increasing the particle resolution. This is because the detection of α_d and previously the unit normal $\hat{\mathbf{n}}$ at the contact line is independent on the particle resolution as the same amount of particles within one cut-off radius is responsible for α_d. The error is given by the relative particle arrangement and therefore given by the geometry of the interface. If you double the particle resolution, halve the particle spacing, the particle arrangement at a given contact angle stays the same as long as you don't introduce an adaptive resolution with more smaller particles belonging to one cut-off radius. Note that there is a trade-off in achieving a constant density field and resolving a thin contact angle with a two-phase interface.

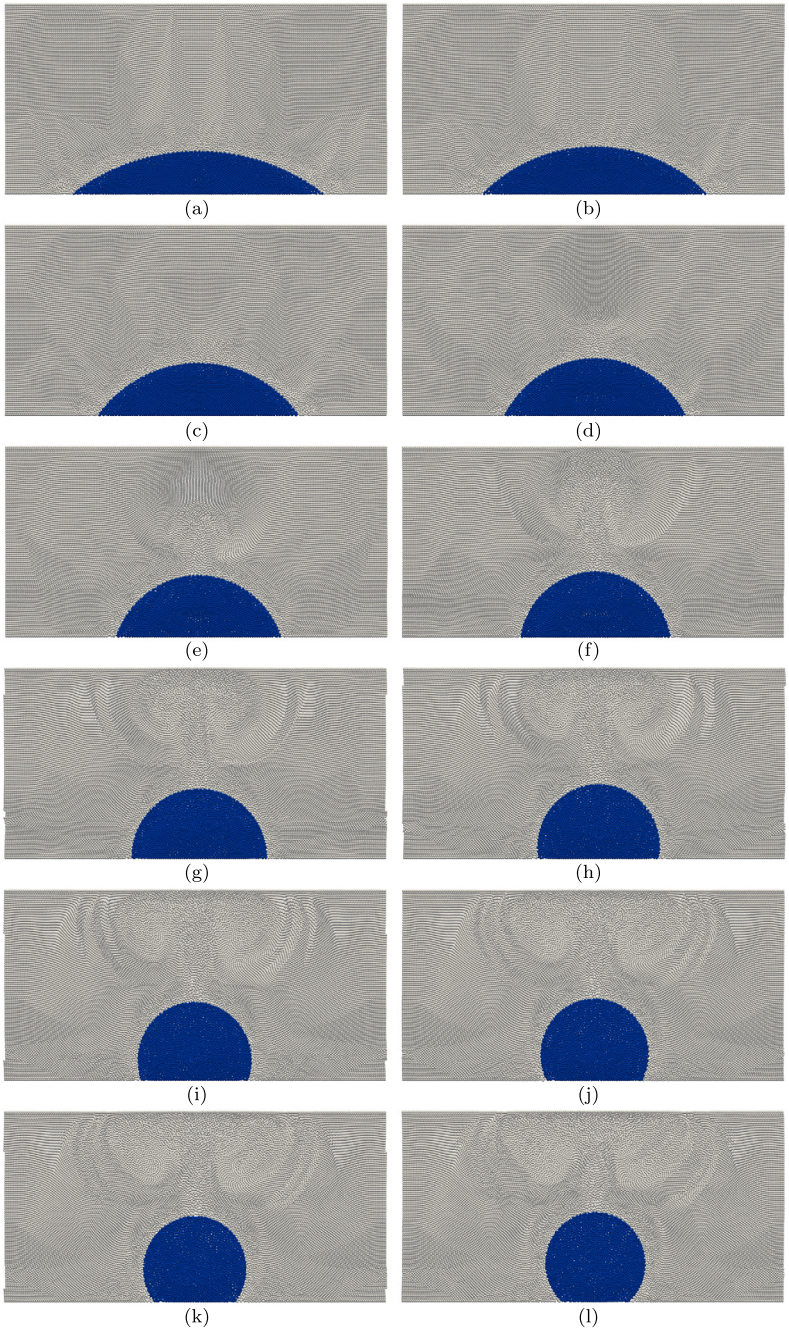

Fig. 10. Equilibrium drop shapes (state after 1 s), evaluated with 20 K particles. Both phases have the same densities $\rho_1 = \rho_2 = 1000$ kg/m^3 and the dynamic viscosities are set to $\mu_1 = \mu_2 = 0.01$ kg/s m. Static contact angles set to (a) 30°, (b) 40°, (c) 50°, (d) 60°, (e) 70°, (f) 80°, (g) 90°, (h) 100°, (i) 110°, (j) 120°, (k) 130° and (l) 140°.

In various simulations different static contact angles are used and each one is simulated with different pressure gradients to obtain steady state advancing and receding contact angles depending on the capillary number, see Fig. 13. Each marker in Fig. 13(a) and Fig. 13(b), respectively, corresponds to one simulation.

In Fig. 14(a) these results are compared to the experiments of Lam et al. [61]. In order to obtain dynamic contact angles, they changed the volume of one drop and looked at the contact angle at the moving contact line. While increasing the volume they measured the advancing contact angle and while decreasing the volume they measured the receding contact angle. Note that due to the linear dependency of the contact angle on the contact line velocity these curves could easily be shifted, but it shows that for a comparable system setup advancing and receding contact angle are similar to the experiment and it reveals the right trend.

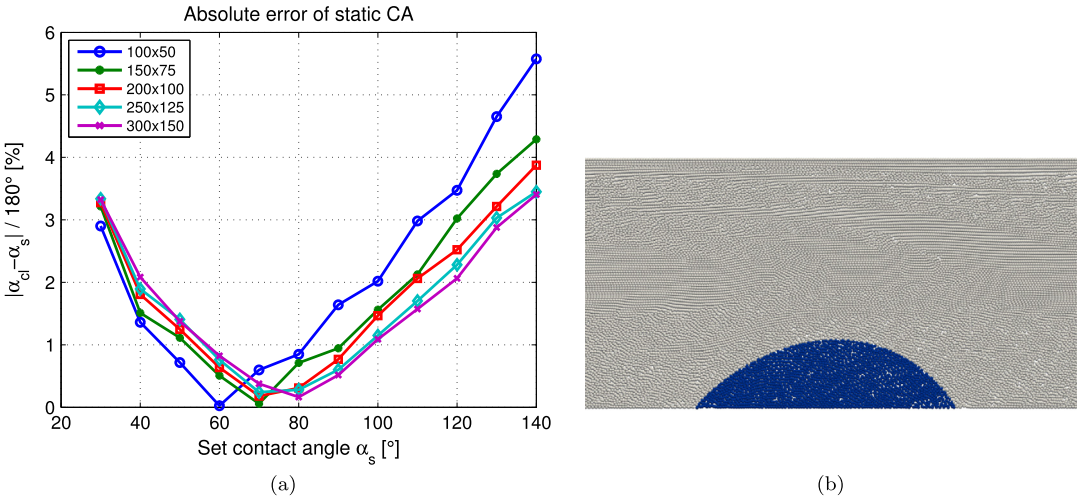

Fig. 11. (a) Absolute error of the static contact angle with respect to the set contact angle using the ghost particle method for different initial particle resolutions. (b) Dynamic drop shape, caused by a motion due to a pressure gradient.

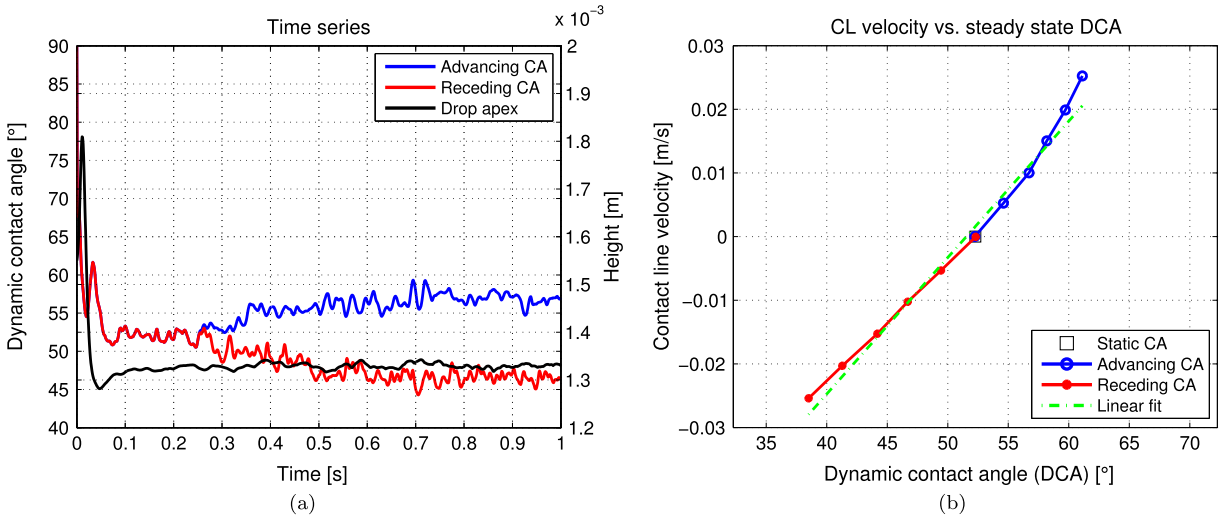

Fig. 12. (a) Evolution of advancing and receding contact angle in time for a static contact angle of $\alpha_s = 50°$ and $\nabla P = -200$ Pa/m. Third black line shows the corresponding evolution of the drop apex. (b) Dependence of the dynamic contact angle on the contact line velocity.

Last but not least a “grid convergence” is shown, where the same simulation is repeated with an increasing amount of particles, cf. Fig. 14(b). Note that, according to Fatehi et al. [62], a grid convergence with an irregular particle distribution may fail as long as no higher order methods are applied, cf. Tartakovsky et al. [63] too.

6. Concluding remarks

A new formulation for dynamic contact angles is proposed in this work. We introduce an indirect formulation of the contact line and use a volume reformulation to transform the force per line to a force per volume. Interfacial forces and Contact Line Forces are jointly used for an extension of the Navier–Stokes equations. Simulations for different static contact angles are carried out and the equilibrium state was verified. Moreover dynamical droplet shapes with advancing and receding contact angles are analyzed. The advantage of this new approach is, that one can apply it for big density ratios using the CSF formulation, as shown by Adami et al. [47]. Moreover the driving force can be easily exchanged in this formalism, if other wetting models are subject of new investigations. No fitting parameters are necessary and where other models apply constitutive equations for the dynamic contact angle or specific slip-models, here, the slip is obtained as a result. Porting the formalism to three dimensions is straightforward.

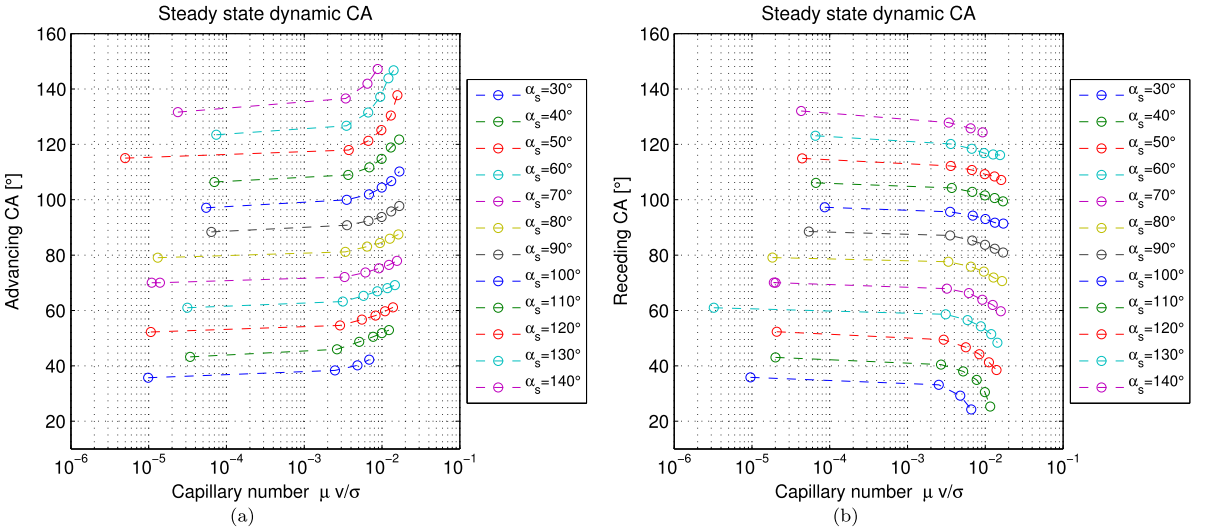

Fig. 13. Steady state dynamic contact angles in dependence of the capillary number, (a) the advancing contact angle and (b) the receding contact angle.

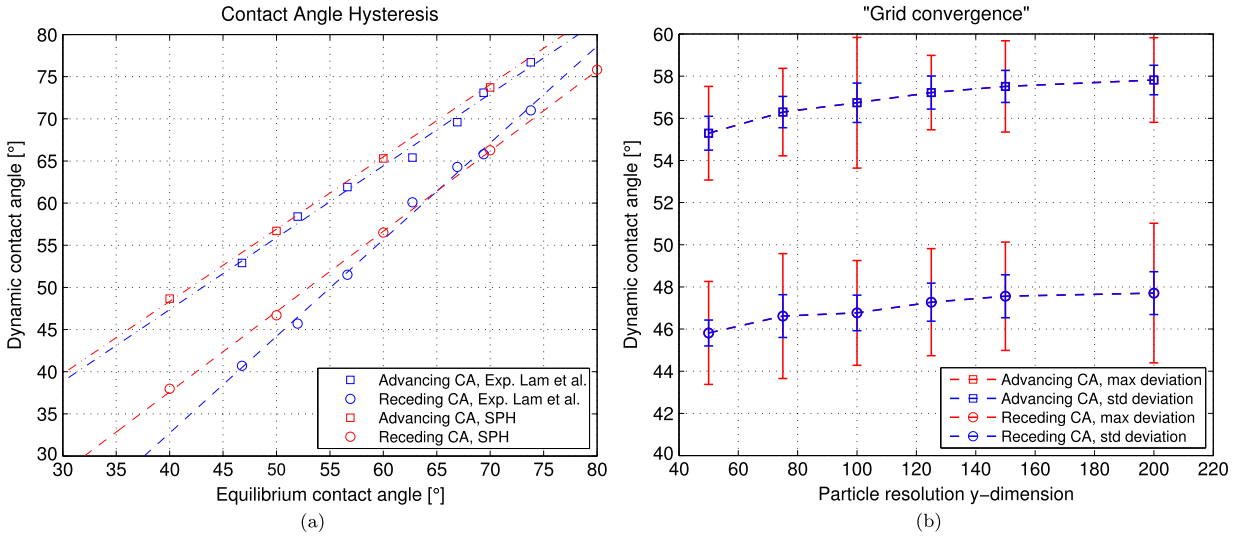

Fig. 14. (a) Advancing and receding contact angles in dependency of the equilibrium contact angle. Experimental values by Lam et al. [61] in blue, SPH simulation in red (SPH results carried out with $\sigma_{wn} = 0.0182$ N/m and $\nabla P = -200$ Pa/m). Dashed lines represent linear fits of the corresponding experimental/simulated values. (b) "Grid convergence" for different particle resolutions and a static contact angle of 50°. Error bars show the maximum deviation and standard deviation with respect to the time averaged mean value. (For interpretation of the references to color in this figure legend, the reader is referred to the web version of this article.)

Acknowledgement

This work was funded by the German Research Foundation (DFG—Deutsche Forschungsgesellschaft) within the framework of the International Research Training Group NUPUS, Non-linearities and upscaling in porous media, (IRTG 1398).

References

[1] R.L. Hoffman, A study of the advancing interface. I. Interface shape in liquid–gas systems, J. Colloid Interface Sci. 50 (2) (1975) 228–241.
[2] T.D. Blake, J.M. Haynes, Kinetics of liquid/liquid displacement, J. Colloid Interface Sci. 30 (3) (1969) 421–423.
[3] P.G. deGennes, Wetting – statics and dynamics, Rev. Mod. Phys. 57 (3) (1985) 827–863.
[4] F. Brochard-Wyart, P.G. deGennes, Dynamics of partial wetting, Adv. Colloid Interface Sci. 39 (1992) 1–11.
[5] Y.D. Shikhmurzaev, Moving contact lines in liquid/liquid/solid systems, J. Fluid Mech. 334 (1997) 211–249.
[6] J.U. Brackbill, D.B. Kothe, C. Zemach, A continuum method for modeling surface-tension, J. Comput. Phys. 100 (2) (1992) 335–354.
[7] J. Liu, S. Koshizuka, Y. Oka, A hybrid particle-mesh method for viscous, incompressible, multiphase flows, J. Comput. Phys. 202 (1) (2005) 65–93.
[8] A. Ferrari, I. Lunati, Direct numerical simulations of interface dynamics to link capillary pressure and total surface energy, Adv. Water Resour. 57 (0) (2013) 19–31.

[9] S. Ravi Annapragada, J.Y. Murthy, S.V. Garimella, Droplet retention on an incline, Int. J. Heat Mass Transf. 55 (5–6) (2012) 1457–1465.
[10] A. Das, P. Das, Equilibrium shape and contact angle of sessile drops of different volumes-computation by SPH and its further improvement by DI, Chem. Eng. Sci. 65 (13) (2010) 4027–4037.
[11] S. Sikalo, H.D. Wilhelm, I.V. Roisman, S. Jakirlic, C. Tropea, Dynamic contact angle of spreading droplets: experiments and simulations, Phys. Fluids 17 (6) (2005) 062103.
[12] T. Breinlinger, P. Polfer, A. Hashibon, T. Kraft, Surface tension and wetting effects with smoothed particle hydrodynamics, J. Comput. Phys. 243 (0) (2013) 14–27.
[13] W.Q. Ren, W.N. E, Boundary conditions for the moving contact line problem, Phys. Fluids 19 (2) (2007) 022101.
[14] A. Tartakovsky, P. Meakin, Modeling of surface tension and contact angles with smoothed particle hydrodynamics, Phys. Rev. E 72 (2) (2005) 026301.
[15] G.Z. Zhou, W. Ge, J.H. Li, A revised surface tension model for macro-scale particle methods, Powder Technol. 183 (1) (2008) 21–26.
[16] K. Mahady, S. Afkhami, L. Kondic, A volume of fluid method for simulating fluid/fluid interfaces in contact with solid boundaries, J. Comput. Phys. 294 (2015) 243–257.
[17] U.C. Bandara, A.M. Tartakovsky, M. Oostrom, B.J. Palmer, J. Grate, C. Zhang, Smoothed particle hydrodynamics pore-scale simulations of unstable immiscible flow in porous media, Adv. Water Resour. 62 (2013) 356–369.
[18] B. Lafaurie, C. Nardone, R. Scardovelli, S. Zaleski, G. Zanetti, Modeling merging and fragmentation in multiphase flows with surfer, J. Comput. Phys. 113 (1) (1994) 134–147.
[19] X. Hu, N. Adams, A multi-phase SPH method for macroscopic and mesoscopic flows, J. Comput. Phys. 213 (2) (2006) 844–861.
[20] S.M. Hassanizadeh, W.G. Gray, Thermodynamic basis of capillary-pressure in porous-media, Water Resour. Res. 29 (10) (1993) 3389–3405.
[21] J.J. Monaghan, Smoothed particle hydrodynamics, Annu. Rev. Astron. Astrophys. 30 (1992) 543–574.
[22] H. Wendland, Piecewise polynomial, positive definite and compactly supported radial functions of minimal degree, Adv. Comput. Math. 4 (1) (1995) 389–396.
[23] J. Bonet, T.S.L. Lok, Variational and momentum preservation aspects of smooth particle hydrodynamic formulations, Comput. Methods Appl. Mech. Eng. 180 (1–2) (1999) 97–115.
[24] L.D. Landau, E.M. Lifshitz, Fluid Mechanics, vol. 6, 2nd edition, Pergamon Press, Headington Hill Hall, Oxford, England, 1987.
[25] G.R. Liu, M.B. Liu, Smoothed Particle Hydrodynamics, World Scientific, 2003.
[26] W. Pan, A.M. Tartakovsky, J.J. Monaghan, Smoothed particle hydrodynamics non-newtonian model for ice-sheet and ice-shelf dynamics, J. Comput. Phys. 242 (2013) 828–842.
[27] A.J. Chorin, Numerical solution of the Navier–Stokes equations, Math. Comput. 22 (104) (1968) 745–762.
[28] R.D. Falgout, U.M. Yang, hypre: a library of high performance preconditioners, in: Preconditioners, in: Lecture Notes in Computer Science, 2002, pp. 632–641.
[29] R. Falgout, J. Jones, U. Yang, The design and implementation of hypre, a library of parallel high performance preconditioners, in: A. Bruaset, A. Tveito (Eds.), Lecture Notes in Computational Science and Engineering, vol. 51, Springer, Berlin, Heidelberg, 2006, pp. 267–294.
[30] S. Balay, S. Abhyankar, M.F. Adams, J. Brown, P. Brune, K. Buschelman, V. Eijkhout, W.D. Gropp, D. Kaushik, M.G. Knepley, L.C. McInnes, K. Rupp, B.F. Smith, H. Zhang, PETSc Web page, http://www.mcs.anl.gov/petsc, 2014.
[31] S. Balay, S. Abhyankar, M.F. Adams, J. Brown, P. Brune, K. Buschelman, V. Eijkhout, W.D. Gropp, D. Kaushik, M.G. Knepley, L.C. McInnes, K. Rupp, B.F. Smith, H. Zhang, PETSc users manual, Tech. Rep. ANL-95/11 - Revision 3.4, Argonne National Laboratory, 2013.
[32] S. Balay, W.D. Gropp, L.C. McInnes, B.F. Smith, Efficient management of parallelism in object oriented numerical software libraries, in: E. Arge, A.M. Bruaset, H.P. Langtangen (Eds.), Modern Software Tools in Scientific Computing, Birkhäuser Press, 1997, pp. 163–202.
[33] L.B. Lucy, Numerical approach to testing of fission hypothesis, Astron. J. 82 (12) (1977) 1013–1024.
[34] R.A. Gingold, J.J. Monaghan, Smoothed particle hydrodynamics – theory and application to non-spherical stars, Mon. Not. R. Astron. Soc. 181 (2) (1977) 375–389.
[35] J.J. Monaghan, Smoothed particle hydrodynamics, Rep. Prog. Phys. 68 (8) (2005) 1703–1759.
[36] S. Rosswog, Astrophysical smooth particle hydrodynamics, New Astron. Rev. 53 (4–6) (2009) 78–104.
[37] J.P. Morris, P.J. Fox, Y. Zhu, Modeling low Reynolds number incompressible flows using SPH, J. Comput. Phys. 136 (1) (1997) 214–226.
[38] K. Szewc, A. Taniere, J. Pozorski, J.P. Minier, A study on application of smoothed particle hydrodynamics to multi-phase flows, Int. J. Nonlinear Sci. Numer. Simul. 13 (6) (2012) 383–395.
[39] A. Colagrossi, M. Landrini, Numerical simulation of interfacial flows by smoothed particle hydrodynamics, J. Comput. Phys. 191 (2) (2003) 448–475.
[40] D.J. Price, Modelling discontinuities and Kelvin–Helmholtz instabilities in SPH, J. Comput. Phys. 227 (24) (2008) 10040–10057.
[41] J.I. Read, T. Hayfield, O. Agertz, Resolving mixing in smoothed particle hydrodynamics, Mon. Not. R. Astron. Soc. 405 (3) (2010) 1513–1530.
[42] X. Hu, N. Adams, An incompressible multi-phase SPH method, J. Comput. Phys. 227 (1) (2007) 264–278.
[43] S. Adami, X. Hu, N. Adams, A transport-velocity formulation for smoothed particle hydrodynamics, J. Comput. Phys. 241 (0) (2013) 292–307.
[44] N. Grenier, M. Antuono, A. Colagrossi, D. Le Touze, B. Alessandrini, An Hamiltonian interface SPH formulation for multi-fluid and free surface flows, J. Comput. Phys. 228 (22) (2009) 8380–8393.
[45] N. Grenier, D. Le Touze, A. Colagrossi, M. Antuono, G. Colicchio, Viscous bubbly flows simulation with an interface SPH model, Ocean Eng. 69 (2013) 88–102.
[46] J.P. Morris, Simulating surface tension with smoothed particle hydrodynamics, Int. J. Numer. Methods Fluids 33 (3) (2000) 333–353.
[47] S. Adami, X.Y. Hu, N.A. Adams, A new surface-tension formulation for multi-phase SPH using a reproducing divergence approximation, J. Comput. Phys. 229 (13) (2010) 5011–5021.
[48] K. Szewc, J. Pozorski, J.P. Minier, Analysis of the incompressibility constraint in the smoothed particle hydrodynamics method, Int. J. Numer. Methods Eng. 92 (4) (2012) 343–369.
[49] S.J. Cummins, M. Rudman, An SPH projection method, J. Comput. Phys. 152 (2) (1999) 584–607.
[50] M. Basa, N.J. Quinlan, M. Lastiwka, Robustness and accuracy of SPH formulations for viscous flow, Int. J. Numer. Methods Fluids 60 (10) (2009) 1127–1148.
[51] T. Belytschko, Y. Krongauz, J. Dolbow, C. Gerlach, On the completeness of meshfree particle methods, Int. J. Numer. Methods Eng. 43 (5) (1998) 785–819.
[52] J.K. Chen, J.E. Beraun, T.C. Carney, A corrective smoothed particle method for boundary value problems in heat conduction, Int. J. Numer. Methods Eng. 46 (2) (1999) 231–252.
[53] G.M. Zhang, R.C. Batra, Modified smoothed particle hydrodynamics method and its application to transient problems, Comput. Mech. 34 (2) (2004) 137–146.
[54] W.K. Liu, S.F. Li, T. Belytschko, Moving least-square reproducing Kernel methods. 1. Methodology and convergence, Comput. Methods Appl. Mech. Eng. 143 (1–2) (1997) 113–154.
[55] G. Bilotta, G. Russo, A. Herault, C. Del Negro, Moving least-squares corrections for smoothed particle hydrodynamics, Ann. Geophys. 54 (5) (2011) 622–633.
[56] S. Adami, X.Y. Hu, N.A. Adams, A generalized wall boundary condition for smoothed particle hydrodynamics, J. Comput. Phys. 231 (21) (2012) 7057–7075.

[57] M. Ferrand, D.R. Laurence, B.D. Rogers, D. Violeau, C. Kassiotis, Unified semi-analytical wall boundary conditions for inviscid, laminar or turbulent flows in the meshless SPH method, Int. J. Numer. Methods Fluids 71 (4) (2013) 446–472.
[58] A. Mayrhofer, B.D. Rogers, D. Violeau, M. Ferrand, Investigation of wall bounded flows using SPH and the unified semi-analytical wall boundary conditions, Comput. Phys. Commun. 184 (11) (2013) 2515–2527.
[59] R. Vacondio, B.D. Rogers, P.K. Stansby, Smoothed particle hydrodynamics: approximate zero-consistent 2-d boundary conditions and still shallow-water tests, Int. J. Numer. Methods Fluids 69 (1) (2012) 226–253.
[60] S. Shao, E.Y.M. Lo, Incompressible SPH method for simulating newtonian and non-newtonian flows with a free surface, Adv. Water Resour. 26 (7) (2003) 787–800.
[61] C.N.C. Lam, R. Wu, D. Li, M.L. Hair, A.W. Neumann, Study of the advancing and receding contact angles: liquid sorption as a cause of contact angle hysteresis, Adv. Colloid Interface Sci. 96 (1–3) (2002) 169–191.
[62] R. Fatehi, M.T. Manzari, Error estimation in smoothed particle hydrodynamics and a new scheme for second derivatives, Comput. Math. Appl. 61 (2) (2011) 482–498.
[63] A. Tartakovsky, N. Trask, K. Pan, B. Jones, W. Pan, J. Williams, Smoothed particle hydrodynamics and its applications for multiphase flow and reactive transport in porous media, Comput. Geosci. (2015) 1–28.